Fractional-order Virtual Inertia Control and Parameter Tuning for Energy-storage System in Low-inertia Power Grid

Yukai Zeng, Qiufan Yang, Yujun Lin, Yin Chen, Xia Chen, *Senior Member*, *IEEE*, and Jinyu Wen, *Member*, *IEEE*

***Abstract*—As conventional synchronous generators are replaced by large-scale converter-interfaced renewable-energy sources (RESs), the electric power grid encounters the challenge of low rotational inertia. Consequently, system frequency deviation is exacerbated and system instability may occur when the frequency deviates beyond the acceptable range. To mitigate this effect, this study proposes a virtual inertia control (VIC) strategy based on a fractional-order derivative and controller parameter-tuning method. The tuning method uses the stability boundary locus and provides a stability criterion for identifying the stability region in the parameter space. The controller parameters are then optimized within the identified stability region to suppress frequency deviation and enhance system robustness. The proposed controller and tuning method is applied to a battery energy-storage system (BESS) in a low-inertia power system with the integration of RESs. Time-domain simulations are carried out to verify the stability region and compare the performance of the optimized proposed controller to that of the traditional integral-order controller. The simulation results show that the stability-analysis method is effective and that the fractional-order VIC, tuned with the proposed method, outperforms the traditional method in both frequency-regulation performance and parametric robustness.**

***Index Terms*—Virtual inertia control, frequency regulation, fractional-order controller, stability region, parameter tuning.**

Received: December 12, 2023
Accepted: May 12, 2024
Published Online: September 1, 2024

Yukai Zeng, Qiufan Yang, Yujun Lin, Xia Chen, and Jinyu Wen are with the State Key Laboratory of Advanced Electromagnetic Engineering, Huazhong University of Science and Technology, Wuhan 430074, China (e-mail: ykzeng417@qq.com; 821737993@qq.com; 672836068@qq.com; cxhust@foxmail.com; jinyu.wen@hust.edu.cn).

Yin Chen (corresponding author) is with the Department of Electronic and Electrical Engineering, University of Strathclyde, Glasgow G11XW, U.K. (e-mail: yin.chen.101@strath.ac.uk).

DOI: 10.23919/PCMP.2023.000111

I. Introduction

In recent years, the scale of renewable-energy sources (RESs) integrated into electrical-power systems through power electronic converters has increased considerably. Unlike conventional synchronous machines, power electronic devices do not inherently store kinetic energy, and they decouple the system frequency from the speed of the rotating machines. Hence, converter-interfaced RESs, such as photovoltaic (PV) generation and doubly fed induction generator (DFIG) wind turbines, neither provide inertial support nor participate in primary frequency regulation. As more conventional synchronous generators are replaced by RESs, the rotational inertia and primary frequency support of power systems will decrease considerably. Consequently, power systems are more prone to frequency instabilities [1], [2].

To address these issues, various approaches have been proposed to improve the frequency-regulation performance and enhance frequency stability. Electrochemical energy-storage systems (ESSs) can provide a fast response and are therefore applicable to fast frequency response (FFR) services, that is, inertial response and primary frequency regulation (PFR) [3]. Hence, the exploitation of ESSs for frequency-regulation services has gained significant attention from both academia and industry. Typical ESSs applied in frequency regulation include batteries, supercapacitors, and superconducting magnetic energy storage.

An effective control scheme for ESSs to provide inertial support and PFR is to implement virtual inertia control (VIC) on the converter to mimic the rotor dynamics of a synchronous machine. Numerous control techniques have been proposed to implement VIC. They can be classified into two categories based on their synchronization modes: grid-following (GFL) and grid-forming (GFM) controls [4]. A typical VIC for the GFM converter is the virtual synchronous generator (VSG) control, in which the controller directly dictates the frequency (or phase) of the output voltage [5], [6]. The GFL converter follows the frequency (or phase) of the voltage at the point of common coupling (PCC) via the phase-lock loop (PLL). Compared with the GFM converter, the GFL converter is more common and

mature at present and is therefore more applicable. For GFL converters, most studies employed droop or derivative control as the VIC algorithm to emulate mechanical inertia [7]–[11]. The converter was controlled to inject active power in proportion to the frequency deviation or rate of change of frequency (ROCOF).

The fractional-order controller (FOC) is a generalized concept of the conventional integer-order controller (IOC). In contrast to the traditional IOC, the order of the derivative or integral in the FOC is a fraction. The FOC has been widely applied in recent studies. In [12], a fractional-order regulator was applied to the active power-control law of a VSG, which significantly improved the inertial and damping effects. Reference [13] designed a fractional order PI^{λ} controller for the two-stage vehicle to grid (V2G) converter, and experiment results verified its effectiveness. In [14], the FOC was implemented in a DC/AC system to provide inertial support for the bus voltage of a DC microgrid. In addition to performance, some studies have applied the FOC to promote control robustness. The FOPID-based outer voltage controller in [15], applied to a microgrid VSC system, outperformed the conventional PI controller. Additionally, more advanced fractional order (FO) control techniques are available. For example, reference [16] proposed a sliding FOC to enhance the robustness of converter-interfaced distributed generation (DG). In [17], a variable FOPID trained online by a neural network was applied to tune the inertia constant of an ESS, thereby improving the frequency-regulation performance. These studies confirmed that with extra tuning degrees of freedom, the FOC always outperforms the traditional IOC in terms of both performance and robustness.

With respect to frequency regulation, a fractional order lead-lag controller was applied to the control loop of an ESS for frequency regulation in [18], and the results showed that the FOC was better than the IOC in terms of dynamic performance. Reference [19] employed FOC for load frequency control (LFC) for interconnected power systems and proposed a novel parameter tuning method based on chaos game optimization. Reference [20] proposes a data-driven adaptive FOC-based virtual inertia and damping control for a GFL DFIG, where the controller parameters were tuned using the gradient-descent method. Most related studies focused on improving the frequency-regulation performance of the VIC. However, few of them focused on the stability analysis and robustness of the controller.

From the viewpoint of system-frequency stability, the VIC must determine the appropriate parameter values. Conservative values reduce the frequency-regulation performance, whereas aggressive values can lead to frequency instability. A widely used offline design method that considers frequency stability involves building a frequency-response model of the power system and determining the stability boundary locus (SBL) in the parameter space [21]. The area enclosed by the SBL curve corresponded to a stable region. The SBL method has also been applied to tune the FOC parameters in [11] and [19]. This method is feasible for frequency-stability analysis. However, the parameter space is divided into numerous parts by the SBL curve. Most studies selected an intuitionally reasonable part as the stability region without any rigorous mathematical proof. In addition, although the parameters are tuned within the stability region, a parameter setpoint close to the stability boundary is typically preferred for a better frequency-regulation performance [20], which makes the controller vulnerable to system disturbances.

Based on the above mentioned issues, this work proposes an FOVIC for battery energy-storage system (BESS) and a parameter-tuning method for the FOVIC. This method uses the SBL method to determine the stability region in the parameter space. In particular, a stability criterion is introduced to the tuning method to identify the stability region. An optimization model is also developed to determine the finest values of the FOVIC parameters within the identified stability region. Time-domain simulations are performed to verify the identified stability region and compare the frequency-regulation performance and robustness of the well-tuned FOVIC and integer order VIC (IOVIC). The significant findings of this study are as follows:

1) Fractional order calculus is applied innovatively to the VIC algorithm. With the introduction of an extra degree of freedom, a well-tuned FOVIC outperforms the traditional IOVIC.

2) Few studies have focused on parameter tuning and the stability analysis of VIC. This study proposes a parameter-tuning method that identifies the stability region of FOVIC in the parameter space, which is the basis of parameter tuning. Moreover, a rigorous mathematical proof is provided to identify the stability region.

3) An optimization model is established to tune the parameters of the FOVIC from the perspective of suppressing frequency deviation and enhancing system robustness. Notably, the robustness of the parameter setpoint is quantized geometrically and included in the optimization model.

The remainder of this paper is structured as follows. In Section II, the description and frequency-response model of the studied power system and BESS are presented. In Section III, the theory and implementation of the FOC are briefly introduced and the FOVIC for the BESS is proposed. Section IV elaborates on the parameter-tuning framework for the FOVIC. Section V presents the parameter tuning results of the FOVIC and two other typical VICs, and compares their frequency-regulation performance and robustness. Section VI concludes the paper.

II. System Modeling

The power system investigated in this study includes conventional power plants, such as reheated thermal power plants and hydraulic power plants. Renewable-energy generation, such as PV generation, is also included. The installed capacity of the genera-

tion system is 550 MW for the thermal power plant, 250 MW for the hydraulic plant, and 200 MW for the PV system. To alleviate the negative effect of RESs on the inertia and damping characteristics of the system, a 100 MW BESS is embedded in the system to provide frequency-regulation services.

A frequency-response model for investigating the frequency stability of the system is depicted in Fig. 1. The parameters and related variables of the studied system are summarized in Table I. The frequency deviation of the power system can be represented as follows:

$$\Delta f = \frac{1}{Ms + D}(\Delta P_{\mathrm{c}} - \Delta P_{\mathrm{L}}^{*} + \Delta P_{\mathrm{BESS}}) \tag{1}$$

where Δf is the frequency deviation; ΔP_{c} is the output power of the conventional plants; $\Delta P_{\mathrm{L}}^{*}$ is the load disturbance; and ΔP_{BESS} is the output power of the BESS.

TABLE I
PARAMETERS OF THE STUDIED POWER SYSTEM

Parameter/Variable	Value
Base power S_{B} (MW)	1000
System inertia M (s)	5
System damping D (MW/Hz)	1.5
Participation factor of thermal and hydraulic power plants P_{th}, P_{hy}	0.55, 0.25
Steam turbine primary droop factor R_{t} (Hz/MW)	0.0025
Steam turbine governor time constant T_{gt} (s)	0.1
Steam turbine reheat time constant T_{rh} (s)	7
Steam turbine reheat constant F_{hp}	0.3
Steam turbine time constant T_{t} (s)	0.4
Hydro turbine primary droop factor R_{h} (Hz/MW)	0.0025
Hydro turbine governor time constant T_{gh} (s)	0.2
Hydro turbine speed governor reset time T_{r} (s)	4.9
Hydro turbine speed governor transient droop time constant T_{td} (s)	28.75
Starting time of water in hydro turbine T_{w} (s)	1.1
Time constant of the inner current loop of BESS T_{ESS} (s)	0.05
Communication delay τ (s)	0.1
Damping ratio of PLL ζ	1.2
Inherent frequency of PLL ω_{n} (Hz)	20
Maximum capacity of ESS P_{ESSM} (p.u.)	0.1

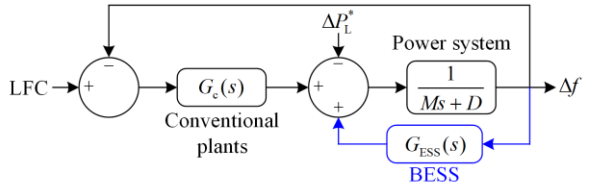

Fig. 1. Frequency-response model of the investigated power system.

A. Conventional Power Plants

The conventional power plants of the investigated system consisted of a reheated thermal power plant and hydraulic power plant, the parameters of which are described in [22]. Because the dynamics of the power-system stabilizer and automatic voltage regulation are relatively fast, the model omits their impact on the low-frequency dynamics. This simplification was verified to be effective in [23]. However, such a model may not be suitable for applications involving fast dynamics [24].

The output power of the conventional plants ΔP_{c} can be represented as follows:

$$\Delta P_{\mathrm{c}} = \Delta P_{\mathrm{t}} + \Delta P_{\mathrm{h}} \tag{2}$$

where ΔP_{t} and ΔP_{h} are the output powers of the thermal and hydraulic power plants, respectively.

The frequency-response model of the thermal and hydraulic plant is given in Fig. 2 [22], and ΔP_{t} and ΔP_{h} can be derived in (3) and (4) according to the model.

$$\Delta P_{\mathrm{t}} = G_{\mathrm{t}}(s)\Delta f = \frac{P_{\mathrm{th}}}{R_{\mathrm{t}}}\left(\frac{1}{T_{\mathrm{gt}}s+1}\cdot\frac{T_{\mathrm{rh}}F_{\mathrm{hp}}s+1}{T_{\mathrm{rh}}s+1}\right)\Delta f \tag{3}$$

$$\Delta P_{\mathrm{h}} = G_{\mathrm{h}}(s)\Delta f = \frac{P_{\mathrm{hy}}}{R_{\mathrm{h}}}\left(\frac{1}{T_{\mathrm{gh}}s+1}\cdot\frac{T_{\mathrm{r}}s+1}{T_{\mathrm{td}}s+1}\cdot\frac{-T_{\mathrm{w}}s+1}{0.5T_{\mathrm{w}}s+1}\right)\Delta f \tag{4}$$

The transfer function of the whole conventional power plant can be represented by:

$$G_{\mathrm{c}}(s) = G_{\mathrm{t}}(s) + G_{\mathrm{h}}(s) \tag{5}$$

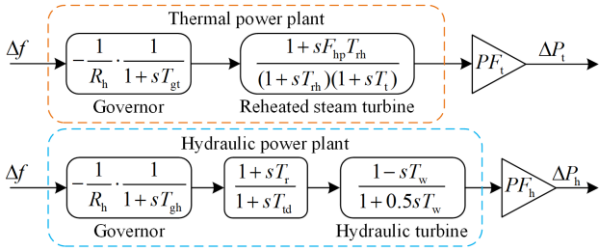

Fig. 2. Model of thermal and hydraulic power plant.

B. PV Generation and Domestic Load

The output power of the PV array is stochastic and fluctuates because it depends on weather conditions. To obtain a realistic output profile of solar-power generation, the output fluctuation can be modelled as the standard deviation multiplied by white noise [25]. The PV generation of the investigated system is controlled to inject maximum power into the power system and does not participate in frequency regulation. Hence, the deviation in PV power generation can be aggregated into an external disturbance of the system with a domestic load.

Similarly, the real-time stochastic power fluctuation in a domestic-load profile can be simulated by multi-

plying the standard deviation by the random output fluctuation of white noise [25]. Eventually, the external disturbance input of the system can be described as the sum of the PV-power generation fluctuation ΔP_{PV} and domestic load variation ΔP_{L}:

$$\Delta P_{\mathrm{L}}^{*} = \Delta P_{\mathrm{L}} + \Delta P_{\mathrm{PV}} \tag{6}$$

C. BESS with VIC

A BESS is installed to provide frequency support, including the inertial response and primary frequency control. The BESS does not provide those services with considerable energy throughput, such as LFC or peak shaving. The BESS only provides an FFR service, which has insignificant energy throughput, and the SOC limit of the BESS is not considered here.

The BESS is connected to the main grid using a GFL converter. A general GFL control structure is described in [26]. The DC/AC converter is controlled to inject real and reactive power into the main grid according to the power setpoints [27]. The power setpoints are determined by a VIC controller that used the measured frequency of the grid as its input. This controller is discussed in detail in the following section. In electromechanical timescale dynamics, the dynamics of the inner current loop can be ignored or reduced to a first-order lag element with a small time constant T_{ESS} [28].

Typically, a PLL is used to synchronize the GFL converter to the grid and measure the grid frequency. The dynamics of the PLL can be approximated using a first- or second-order transfer function [29]. This study adopts a second-order transfer function:

$$G_{\mathrm{PLL}}(s) = \frac{2\zeta\omega_{\mathrm{n}}s + \omega_{\mathrm{n}}^{2}}{s^{2} + 2\zeta\omega_{\mathrm{n}}s + \omega_{\mathrm{n}}^{2}} \tag{7}$$

where ζ and ω_{n} are the damping ratio and inherent frequency, respectively.

In most studies related to VIC, the control algorithm is implemented within the DSP-based digital controller of the power converters. However, such an implementation can lead to difficulty in upgrading the control algorithms in the DSP-based controller and incur additional development efforts and costs. Hence, reference [30] proposed an external controller that implemented the VIC algorithm. The external controller, such as the front-end PLC of the power converters, communicates with the DSP-based controller via a standard communication link. Such a PLC is already available in most commercial power converters and is more economical than embedding a control algorithm in the converter controller [31]. Because communication between the front-end PLC and DSP-based controller is introduced, communication delays inevitably occur. The delay time depends on the communication protocol, network condition, and topology and is often in the range of a few to dozens of milliseconds [32]. This study adopts the above-mentioned external control method. Thus, the communication delay in the control loop must be considered in the model.

In conclusion, the active power-control loop of the BESS comprises a communication delay, PLL, VIC controller, and an inner current loop. The frequency-response characteristics of the BESS can be described by the model shown in Fig. 3, and the transfer function of the BESS can be represented by (8), where $G_{\mathrm{VIC}}(s)$ is the transfer function of the virtual inertia controller introduced in Section III.

$$G_{\mathrm{ESS}}(s) = \frac{\mathrm{e}^{-\tau s}}{T_{\mathrm{ESS}}s + 1} \cdot \frac{2\zeta\omega_{\mathrm{n}}s + \omega_{\mathrm{n}}^{2}}{s^{2} + 2\zeta\omega_{\mathrm{n}}s + \omega_{\mathrm{n}}^{2}} G_{\mathrm{VIC}}(s) \tag{8}$$

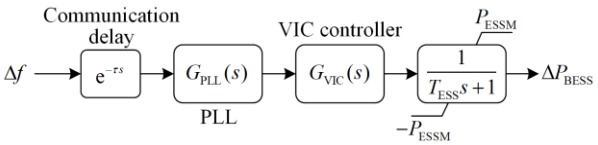

Fig. 3. Model of BESS.

III. Fractional-order Virtual Inertia Control

An FOVIC that possesses better dynamic performance and robustness than a conventional IOVIC based on an integer-order derivative operator is proposed in this section.

A. Essentials of Fractional-order Control

The fractional differentiation extends the powers of the differentiation operator $(\mathrm{d}^{n}/\mathrm{d}t^{n}, n \in \mathbb{N})$ to real or complex number powers. Several definitions of fractional differentiation exist, including the Riemann-Liouville (R-L), Caputo, and Grünwald-Letnikov (G-L) definitions [33]. Because the fractional algorithm is implemented in a digital controller, a definition in discrete form, which is the G-L definition, would be more suitable. The G-L fractional-order derivative definition is the generalized form of the Cauchy order $n \in \mathbb{N}$ derivative and is expressed as follows:

$$\frac{\mathrm{d}^{v} f(t)}{\mathrm{d}^{v} t} = \lim_{\substack{h \to 0 \\ l \to +\infty}} \frac{\sum_{k=0}^{l} (-1)^{k} \binom{v}{k} f(t - kh)}{h^{v}} \tag{9}$$

where v is the order of the derivative; h is the sampling time; and $\binom{v}{k}$ is the generalized Newton binomial coefficient, given by:

$$\binom{v}{k} = \frac{\Gamma(v+1)}{k!\,\Gamma(v-k+1)} \tag{10}$$

Notably, calculating $\binom{v}{k}$ according to (10) in the DSP program exceeds the range of floating-point numbers because $k!$ increases steeply. Hence, a recur-

sion formula is provided in (11) to address this problem and the proof of the formula is provided in [34].

$$w_k=(-1)^k\binom{v}{k}=\begin{cases}1, & k=0\\ \left(1-\dfrac{v+1}{k}\right)w_{k-1}, & k=1,2,\cdots\end{cases} \tag{11}$$

Similarly, the conventional integer-order proportional derivative (IOPD) controller can be generalized using fractional-order derivatives. Replacing the Laplacian operator s by its fractional powers s^v, the classic PD controller becomes PD^{μ} defined by:

$$C(s)=K_{\mathrm{p}}+K_{\mathrm{d}}s^v \tag{12}$$

where K_{p} and K_{d} are the proportional and derivative gains, respectively.

B. Fractional-order PD-based VIC

In some studies, most conventional VICs provided an inertial effect by responding to frequency variations of the grid. In general, a derivative term is adopted in the VIC algorithm to provide an active power reference for the control loop of the power conversion system (PCS), and the output power of the BESS changes accordingly. Some studies have also proposed the concurrent imitation of virtual inertia and damping, simultaneously providing both. Such an imitation of virtual inertia and damping is typically realized by a VIC algorithm comprising both proportional and derivative terms, which is a PD controller.

Compared with the IOPD, the fractional-order PD (FOPD) controller possesses an extra degree of freedom. Therefore, the FOPD always outperforms the IOPD in terms of dynamic response and robustness, as long as the controller parameters are well tuned. To enhance the system-frequency stability and robustness, an FOPD was adopted as the VIC algorithm rather than an IOPD. The structure of the VIC controller block is shown in Fig. 4, where J_{v} and D_{v} are the gains of virtual inertia and damping control, respectively. The transfer function of the FOVIC is expressed as:

$$G_{\mathrm{VIC}}(s)=-(J_{\mathrm{v}}s^v+D_{\mathrm{v}}) \tag{13}$$

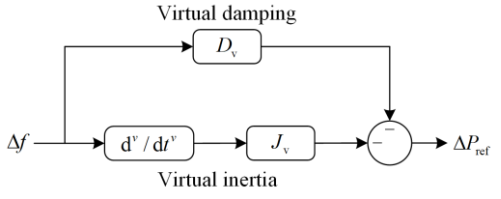

Fig. 4. Block diagram of FOVIC.

IV. Stability Analysis and Parameter Tuning

This section proposes a framework for tuning the controller parameters. The stable region of the FOPD-based VIC, or FOVIC, is determined using the SBL method and proved mathematically. An optimization model is also proposed to determine the finest value of $(J_{\mathrm{v}}, D_{\mathrm{v}}, v)$ that enables the BESS with VIC to provide superior frequency support for the system while retaining a certain stability margin.

The transfer function of every element in the studied system is obtained, and the transfer function from the system disturbance to the frequency response of the system is derived from (1):

$$\frac{\Delta f}{\Delta P_{\mathrm{L}}^*}=-\frac{1}{Ms+D+G_{\mathrm{ESS}}(s)-G_{\mathrm{c}}(s)} \tag{14}$$

The characteristic equation of the system is the denominator of the transfer function and can be expressed as (15). $P(s)$ and $Q(s)$ are polynomials in s with real coefficients. The coefficients of the two polynomials can be deduced using a simple bracket expansion. $e^{-s\tau}$ is introduced based on the communication delay shown in Fig. 3.

$$\begin{cases}\Delta(s)=P(s)+Q(s)(J_{\mathrm{v}}s^v+D_{\mathrm{v}})\mathrm{e}^{-s\tau}\\ P(s)=p_0+p_1s+p_2s^2+p_3s^3+p_4s^4+p_5s^5+\\ \qquad p_6s^6+p_7s^7+p_8s^8+p_9s^9+p_{10}s^{10}\\ Q(s)=q_0+q_1s+q_2s^2+q_3s^3+q_4s^4+q_5s^5+\\ \qquad q_6s^6+q_7s^7\end{cases} \tag{15}$$

A. Stability Boundary Locus

The SBL curve is the set of $(J_{\mathrm{v}}, D_{\mathrm{v}})$ that satisfies (16) when ω is swept from zero to positive infinity.

$$\Delta(\omega,J_{\mathrm{v}},D_{\mathrm{v}})=P(\mathrm{j}\omega)+Q(\mathrm{j}\omega)[J_{\mathrm{v}}(\mathrm{j}\omega)^v+D_{\mathrm{v}}]\mathrm{e}^{-\mathrm{j}\omega\tau}=0 \tag{16}$$

To solve the above equation, the characteristic equation (15) should be rearranged using:

$$\begin{cases}(\mathrm{j}\omega)^v=|\omega|^v\,\mathrm{e}^{\mathrm{j}\omega\frac{\pi}{2}}\\ \mathrm{e}^{-\mathrm{j}\omega\tau}=\cos(\omega\tau)-\mathrm{j}\sin(\omega\tau)\end{cases} \tag{17}$$

After replacing the relevant elements with the above statements, equation(15) can be divided into real and imaginary parts, as follows:

$$\begin{aligned}\Delta(\omega,J_{\mathrm{v}},D_{\mathrm{v}},v)=&J_{\mathrm{v}}A_1(\omega,v)+D_{\mathrm{v}}B_1(\omega,v)+P_1(\omega)+\\ &\mathrm{j}(J_{\mathrm{v}}A_2(\omega,v)+D_{\mathrm{v}}B_2(\omega,v)+P_2(\omega))\end{aligned} \tag{18}$$

where

$$\begin{cases}A_1(\omega,v)=\omega^v\left[Q_1\cos\left(\dfrac{v\pi}{2}-\omega\tau\right)-Q_2\sin\left(\dfrac{v\pi}{2}-\omega\tau\right)\right]\\ A_2(\omega,v)=\omega^v\left[Q_2\cos\left(\dfrac{v\pi}{2}-\omega\tau\right)+Q_1\sin\left(\dfrac{v\pi}{2}-\omega\tau\right)\right]\\ B_1(\omega,v)=Q_1\cos(\omega\tau)+Q_2\sin(\omega\tau)\\ B_2(\omega,v)=Q_2\cos(\omega\tau)-Q_1\sin(\omega\tau)\\ P_1(\omega)=p_0-p_2\omega^2+p_4\omega^4-p_6\omega^6+p_8\omega^8-p_{10}\omega^{10}\\ P_2(\omega)=p_1\omega-p_3\omega^3+p_5\omega^5-p_7\omega^7+p_9\omega^9\\ Q_1(\omega)=q_0-q_2\omega^2+q_4\omega^4-q_6\omega^6\\ Q_2(\omega)=q_1\omega-q_3\omega^3+q_5\omega^5-q_7\omega^7\end{cases} \tag{19}$$

By individually equalizing the real and imaginary parts of (18) to zero, we obtain:

$$\begin{cases} J_{\mathrm{v}} = \dfrac{B_2(\omega,v)P_1(\omega) - B_1(\omega,v)P_2(\omega)}{A_2(\omega,v)B_1(\omega) - A_1(\omega,v)B_2(\omega,v)} \\ D_{\mathrm{v}} = \dfrac{B_1(\omega,v)P_2(\omega) - B_2(\omega,v)P_1(\omega)}{A_2(\omega,v)B(\omega) - A_1(\omega,v)B_2(\omega,v)} \end{cases} \tag{20}$$

The characteristic equation has two stability boundaries on the J_{v}-D_{v} plane under a fixed fractional order v: the real root boundary (RRB) and complex root boundary (CRB). When ω is swept from 0 to positive infinity, RRB and CRB can be plotted. The SBL curve for the studied system is shown in Fig. 5 for $v = 0.1$ and $\tau = 0.1\,\mathrm{s}$.

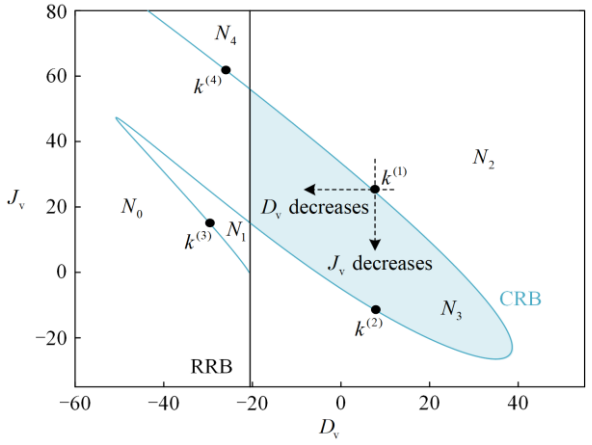

Fig. 5. SBL curve of the studied system for $v = 0.1$ and $\tau = 0.1\,\mathrm{s}$.

B. Stability-region Identification

As shown in Fig. 5, the J_{v}-D_{v} plane is divided into many parts, including N_0, N_1, N_2, etc., by the RRB and CRB. Mathematical methods are introduced to identify the stability region in the parameter plane where the system can remain stable. The stability criterion of the fractional-order system is presented in [35].

Lemma 1. The system is described by a fractional-order quasi-polynomial:

$$\Delta(s, J_{\mathrm{v}}, D_{\mathrm{v}}) = P(s) + Q(s)[J_{\mathrm{v}}(\mathrm{j}\omega)^{v} + D_{\mathrm{v}}]\mathrm{e}^{-s\tau} \tag{21}$$

The system is stable if and only if all zeros w^* of the transformed equation $\Delta(w, J_{\mathrm{v}}, D_{\mathrm{v}}) = P(w) + Q(w)[J_{\mathrm{v}} w + D_{\mathrm{v}}]\,\mathrm{e}^{-w^{1/v}\tau}$, where $w = s^{v}$, satisfy:

$$|\arg(w^*)| > \frac{v\pi}{2} \tag{22}$$

This lemma can also be illustrated on a complex plane, such as in Fig. 6. When all zeros of the transformed characteristic equation lie in the white area, the system is stable.

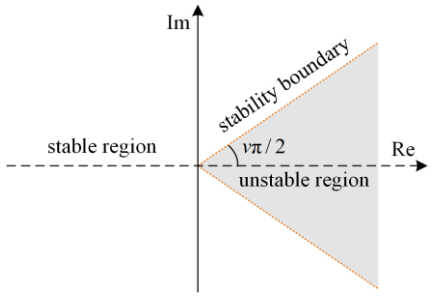

Fig. 6. Stability region of the fractional-order system.

Based on the lemma, a further conclusion was proposed in [36] which helped us determine the stability region on the J_{v}-D_{v} plane.

Lemma 2. Consider the transformed characteristic equation $\Delta(w, J_{\mathrm{v}}, D_{\mathrm{v}}) = P(w) + Q(w)(J_{\mathrm{v}} w + D_{\mathrm{v}})e^{-w^{1/v}\tau}$, and note that $\boldsymbol{k} = (J_{\mathrm{v}}, D_{\mathrm{v}})$. One root of Δ will cross through the zeros from the left to the right of the stability boundary as $\boldsymbol{k}$ crosses the SBL curve on the J_{v}-D_{v} plane through $\boldsymbol{k}^*$ in the increasing direction of J_{v} or D_{v} if

$$S_X(w^*, \boldsymbol{k}^*) > 0 \tag{23}$$

where $\boldsymbol{k}^*$ is a point on the SBL curve, $X \in \{J, D\}$, and S_J and S_D denote the root sensitivity to J_{v} and D_{v}, respectively. $S_X(w^*, \boldsymbol{k}^*)$ can be calculated as follows:

$$\begin{aligned} S_X(w^*, \boldsymbol{k}^*) &= \mathrm{Re}\left\{ \mathrm{e}^{\mathrm{j}\frac{(1-v)\pi}{2}} \left.\frac{\mathrm{d}w}{\mathrm{d}X_{\mathrm{v}}}\right|_{(w^*, \boldsymbol{k}^*)} \right\} = \\ &\mathrm{Re}\left\{ \left.\frac{\mathrm{d}w}{\mathrm{d}X_{\mathrm{v}}}\right|_{(w^*, \boldsymbol{k}^*)} \right\} \sin\frac{v\pi}{2} - \mathrm{Im}\left\{ \left.\frac{\mathrm{d}w}{\mathrm{d}X_{\mathrm{v}}}\right|_{(w^*, \boldsymbol{k}^*)} \right\} \cos\frac{v\pi}{2} \end{aligned} \tag{24}$$

where

$$\begin{cases} \dfrac{\mathrm{d}w(J_{\mathrm{v}}, D_{\mathrm{v}})}{\mathrm{d}X_{\mathrm{v}}} = -\dfrac{\partial\Delta(w, J_{\mathrm{v}}, D_{\mathrm{v}})}{\partial X_{\mathrm{v}}} \Big/ \dfrac{\partial\Delta(w, J_{\mathrm{v}}, D_{\mathrm{v}})}{\partial w} \\ \dfrac{\partial\Delta(w, J_{\mathrm{v}}, D_V)}{\partial J_{\mathrm{v}}} = w\mathrm{e}^{-w^{1/v}\tau} \\ \dfrac{\partial\Delta(w, J_{\mathrm{v}}, D_{\mathrm{v}})}{\partial D_{\mathrm{v}}} = \mathrm{e}^{-w^{1/v}\tau} \\ \dfrac{\partial\Delta(w, J_{\mathrm{v}}, D_{\mathrm{v}})}{\partial w} = \dfrac{P'(w)Q(w) - P(w)Q'(w)}{Q(w)^2} + \\ \qquad J_{\mathrm{v}}\mathrm{e}^{-w^{1/v}\tau} - \dfrac{\tau}{v} w^{1/v-1}\mathrm{e}^{-w^{1/v}\tau}(J_{\mathrm{v}} w + D_{\mathrm{v}}) \end{cases} \tag{25}$$

This lemma determines the system stability according to the root sensitivity to the controller parameters. If the root crosses the imaginary axis from the left half to the right half of the complex plane or $S_X(w^*, \boldsymbol{k}^*) > 0$, the

system is unstable because some of its roots lie on the right-half plane (RHP).

Points on each line that form a closed curve with the RRB are selected and the root sensitivities to J_v and D_v are calculated, that is, S_J and S_D, on these points. From the sign of the root sensitivities, the stability of each closed region can be judged according to Lemma 2: if the S_J value of point $\boldsymbol{k}^*$ is positive, it indicates that when $\boldsymbol{k}^*$ moves towards the direction in which J_v increases, one root of the transformed characteristic equation moves into the unstable region, as shown in . Consequently, the system is unstable when J_v is on the upper side of $\boldsymbol{k}^*$ in the J_v-D_v plane. Similarly, if the S_D value of point $\boldsymbol{k}^*$ is positive, we similarly conclude that the system is unstable when D_v is on the right side of $\boldsymbol{k}^*$. Hence, a stability criterion can be derived.

For a region enclosed by the RRB and CRB, consider sensitivities S_J and S_D of point $\boldsymbol{k}^*$ in the CRB. If S_J or S_D are negative when J_v or D_v change towards the interior of this region, this region is stable.

For example, we consider the stability of region N_3 in Fig. 5 and calculate the sensitivities of point $k^{(1)}$. If S_J or S_D are negative when J_v or D_v change towards the interior of N_3, that is, J_v or D_v decrease, N_3 is the stability region. If the sensitivities of any points do not meet the stability criterion, the region is unstable. In the stable region, the sensitivity of each point on the CRB boundary can satisfy the stability criterion. Therefore, identifying the stability region using this stability criterion is simple.

C. Parameter-optimization Model

The parameters of the fractional controller have a significant impact on the effectiveness of virtual inertia and damping. A comprehensive optimization model is required to finely tune the controller parameters (J_v, D_v, v).

Because the aim of VIC is to suppress frequency deviation, the objective function of the optimization model should include the frequency deviation multiplied by a high weighting factor. A widely used performance index is the integral of the squared error (ISE), which is defined as:

$$I_1 = \int_0^T (\Delta f)^2 \mathrm{d}t \tag{26}$$

The timescales of the inertial and primary frequency responses are typically within 30 s [37]. Therefore, the integral time T is set to 30 s. In general, the output power of the BESS is considered in the objective function in the form of an integral of the squared deviation of the control output (ISDCO), which is defined as follows:

$$I_2 = \int_0^T (\Delta P_{\mathrm{BESS}})^2 \mathrm{d}t \tag{27}$$

In addition, to achieve a lower ISE, a higher value of the controller parameters (J_v, D_v) is preferred, which often lies near the boundary of the stability region or SBL curve. However, in scenarios in which the system parameters undergo significant variations, such (J_v, D_v) values are likely to fall outside the stability region, thereby posing a significant threat to the robustness of the system. Geometrically, the most likely point to remain within the stability region in the case of system-parameter variation is the geometric center of the stability region. Hence, from the perspective of enhancing system robustness, (J_v, D_v) should preferably be set at the centroid of the stability region. To avoid the degradation of robustness, the distance d from the parameter setpoint (J_v, D_v) to the center of the stability region should also be included in the objective function, and d is given as follows:

$$d = \sqrt{(J_v - C_J)^2 + (D_v - C_D)^2} \tag{28}$$

where (C_J, C_D) is the geometric centroid of the stability region. The SBL curve depicted in Fig. 5 is actually approximated by a polygon consisting of the line segments between n vertices (J_v, j, D_v, j), j is from 0 to $(n-1)$. Thus, the centroid can be calculated using the centroid formula for a polygon [38]:

$$\begin{cases} C_D = \dfrac{1}{6A}\displaystyle\sum_{j=0}^{n-1}(D_{v,j} + D_{v,j+1})(D_{v,j}J_{v,j+1} - D_{v,j+1}J_{v,j}) \\ C_J = \dfrac{1}{6A}\displaystyle\sum_{j=0}^{n-1}(J_{v,j} + J_{v,j+1})(D_{v,j}J_{v,j+1} - D_{v,j+1}J_{v,j}) \end{cases} \tag{29}$$

where

$$A = \frac{1}{2}\sum_{j=0}^{n-1}(D_{v,j}J_{v,j+1} - D_{v,j+1}J_{v,j}) \tag{30}$$

Overall, the objective function comprises the ISE, ISDCO, and d. The optimization model can be expressed as:

$$\begin{cases} \min\limits_{J_v, D_v, v} J = w_1 I_1 + w_2 I_2 + w_3 d \\ \text{s.t.} \quad (J_v, D_v) \in \mathscr{R}(v),\ 0 < v < 1.5 \end{cases} \tag{31}$$

where w_1, w_2, and w_3 are the weighting factors and $\mathscr{R}(v)$ is the stability region of (J_v, D_v) under fractional order v. Notably, the system tends to be unstable under excessive v, therefore, this value is limited to the range of (0, 1.5). The optimization model is solved offline using the particle-swarm optimization (PSO) algorithm. This study primarily focuses on identifying the stability region and formulating the optimization model, and the optimization model is solved offline. Thus, the details of the optimization are not elaborated in this study. See reference [39] for the detailed optimization process.

Every step of the procedure for the proposed parameter-tuning method has been presented. Figure 7 shows a flowchart of the proposed tuning method.

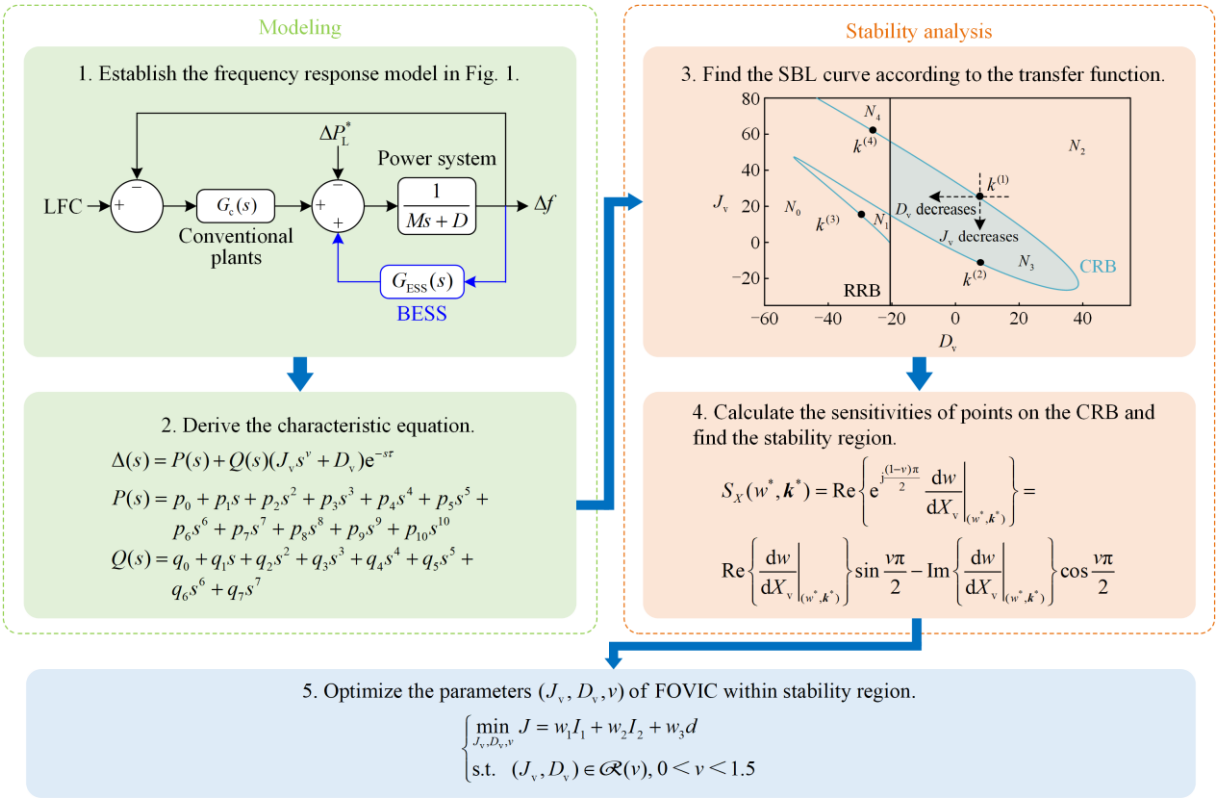

Fig. 7. Flowchart of the proposed parameter-tuning method for FOVIC.

V. Case Study

In this section, a time-domain simulation and analysis are performed in Matlab/Simulink to verify the effectiveness of the FOVIC and proposed parameter-tuning method. The sampling time in Simulink is set to $5e^{-4}$ s, and the solver is ode3 (Bogacki-Shampine method).

A. Stability-region Identification

As shown in Fig. 6, the SBL curves of the characteristic equation (15) under $v=0.1$ are depicted according to (19) and (20). Four points on the curve are selected, denoted as $k^{(1)}$, $k^{(2)}$, $k^{(3)}$, and $k^{(4)}$. The S_J and S_D values of these points are calculated according to (24) and (25), and the results are summarized in Table II. The S_J and S_D values of $k^{(1)}$ are both positive; thus, region N_2 is unstable according to the abovementioned stability criterion. Similarly, we can conclude that regions N_0, N_1, and N_4 are all unstable. The S_J and S_D values of $k^{(1)}$ are positive, whereas those of $k^{(2)}$ are negative, indicating that the painted region N_3 is the stability region.

The behavior of S_J and S_D near knee points *a* and *b* of the SBL curve presented in Fig. 8 confirms the conclusions. Figure 8(b) shows that the sign of S_J changes from negative to positive at knee point *a* as J_v increases. This suggests that the regions above the lower part of the SBL (purple line) and below the upper part of the SBL (orange line) are stable. A similar conclusion can be inferred from Fig. 8(c), which shows that the region above knee point *b* is stable. Every point on the CRB boundary of N_3 meet the stability criterion. Thus, N_3 is rigorously proven to be a stable region.

We now verify the correctness of the identified stability region. Three points are selected: $k^{(5)}=(7.61,20)$, $k^{(6)}=(11.61,20)$, and $k^{(7)}=(9.61,20)$, which are located inside, outside, and at the boundary of N_3. The corresponding frequency responses of the studied power system subject to a 0.01 p.u. load perturbation for $k^{(5)}$, $k^{(6)}$, and $k^{(7)}$ are presented in Fig. 9, which are convergent, divergent, and oscillatory, respectively. The responses further verified the identified stability region.

Similarly, the stability region $\mathscr{R}(v)$ on the J_v-D_v plane of the studied system under any fractional-order $v\in(0,1.5)$ can be determined, which serves as the basis for the following parameter tuning. The stability region under different v values is represented by the space enclosed by the painted surface and RRB in Fig. 10. After identifying the stability region in the parameter space, the optimized parameters for FOVIC can be obtained by solving the optimization model shown by (31).

TABLE II
ROOT SENSITIVITY OF POINTS ON SBL CURVE

Point	$k^{(1)}$	$k^{(2)}$	$k^{(3)}$	$k^{(4)}$
J_v	23.3991	−12.3861	15.6008	6.1893
D_v	8.7871	8.7871	−30.0113	−24.1132
ω	4.6840	1.1080	0.0081	5.3550
S_J	6.3638×10^{-4}	−0.0081	0.0279	7.2883×10^{-4}
S_D	7.5203×10^{-4}	−0.0064	0.0432	7.6737×10^{-4}

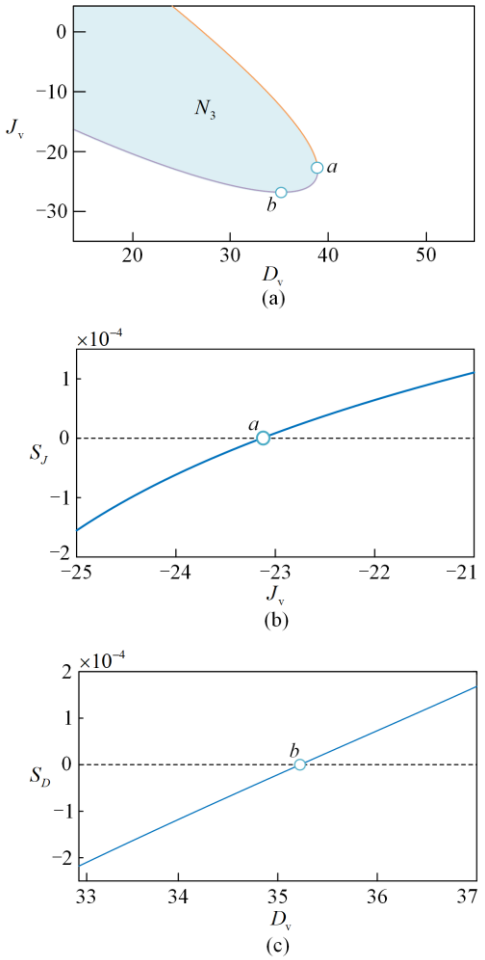

Fig. 8. S_J and S_D behavior near the inflection points. (a) Detailed view of Fig. 6. (b) S_J behavior near knee point *a*. (c) S_D behavior near knee point *b*.

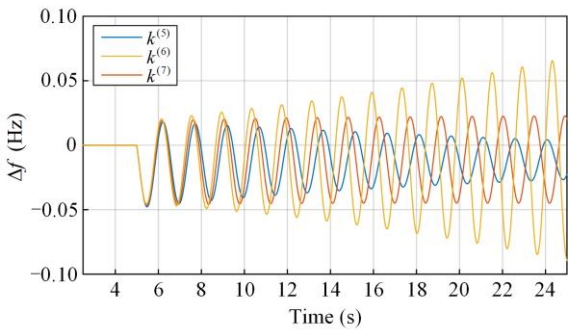

Fig. 9. System frequency response subject to a 0.5% load perturbation.

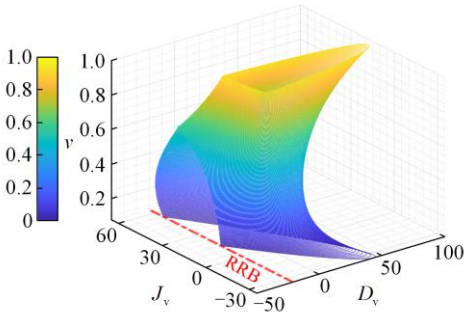

Fig. 10. Stability region of FOVIC in parameter space.

B. Parameter Tuning and Controller Performance

The different values of (J_v, D_v, v) of the FOVIC have a significant influence on its frequency regulation performance. Increasing the virtual inertia J_v improves the dynamic performance by reducing the frequency nadir and deviation during the transient phase, whereas an excessive increase in J_v degrades the settling performance. Virtual damping D_v improves the settling performance and marginally attenuates the transient frequency deviation; however, an aggressive D_v value can lead to large secondary overshoots [11]. The fractional-order v also influences FOVIC performance. As shown in Fig. 11, the frequency nadir and ROCOF decrease as v increases. However, a high v value may also lead to instability. Hence, the values of (J_v, D_v, v) must be comprehensively optimized, for which a novel parameter-tuning method is proposed in this study.

The FOVIC is optimized using the proposed tuning method. In addition, the widely used droop VIC (i.e., $J_v = 0$) and IOVIC (i.e., $v = 0$) are optimized in the same manner. The optimization results of the three controllers are presented in Table III.

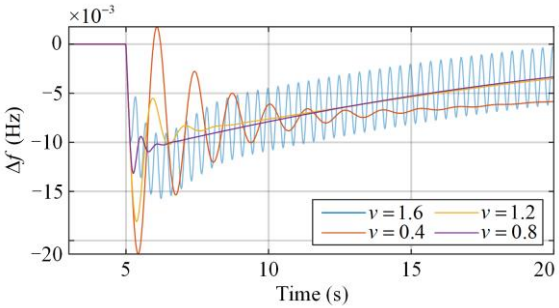

Fig. 11. Frequency response with different fractional order.

TABLE III
CONTROLLER PARAMETER-OPTIMIZATION RESULTS

Controller	J_v	D_v	v	J
Droop VIC	0	15.1274	1	0.0078
Integral-order VIC	6.6141	30.5018	1	0.0038
Fractional-order VIC	7.5181	35.7871	1.0792	0.0031

The performances of the three well-tuned controllers are compared in Table III. The frequency response of the investigated power system under different optimized controller parameters subjected to a 0.5% load-step change is shown in Fig. 12. As expected, a considerable frequency decrease (–0.07 Hz) occurs in the low-inertia power system without a VIC controller. This deviation is significantly alleviated when a BESS with a VIC controller is connected to the grid. Compared with the droop VIC (–0.029 Hz) and IOVIC (–0.017 Hz), the FOVIC controller raises the frequency nadir (–0.012 Hz), and hence decelerates the ROCOF and provides better frequency support. Moreover, both the FOVIC and IOVIC outperform the droop VIC in transient dynamics. This is attributed to their derivative term, which magnifies the output of the BESS during the transient process and reduces the ROCOF. In the steady state, besides LFC, Δf is mainly determined by the proportional item, i.e., the D_v value. Δf tends to be smaller with a larger D_v, which also indicates a higher output of BESS at the steady state.

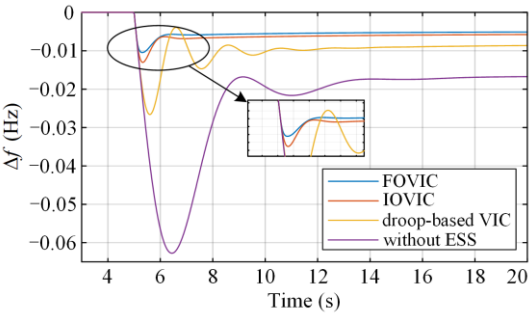

Fig. 12. Frequency response of the studied power system under different optimized controllers subject to a 0.5% load perturbation.

In fact, the FOVIC is likely to outperform the conventional droop VIC and IOVIC. Figure 10 shows that as v increases, the stability region moves upward on the J_v-D_v plane. As v increases, a higher parameter value is available, and a better frequency-regulation performance can be achieved. However, an excessive v value also leads to a smaller stability region, and hence, less robustness. The optimization method achieves a tradeoff between frequency-regulation performance and robustness. Because FOVIC has three degrees of tuning freedom, it outperforms those with one or two degrees of freedom.

To further compare their performances, a simulation is conducted considering the stochastic fluctuation of PV generation and domestic load; the related data were generated according to Section II. The profiles of domestic load and solar-power generation are shown in Fig. 13(a), and they are aggregated into ΔP_L^* as the external-disturbance input of the studied system. The frequency response under these disturbances is shown in Fig. 13(b). The maximum frequency deviations under droop-based VIC, IOVIC, and FOVIC VIC reach ±0.179 Hz, ±0.152 Hz, and ±0.098 Hz, and the ISEs of the frequencies are 0.150, 0.064, and 0.046, respectively. The ROCOF is significantly reduced, and the frequency deviation is better alleviated under the effect of FOVIC.

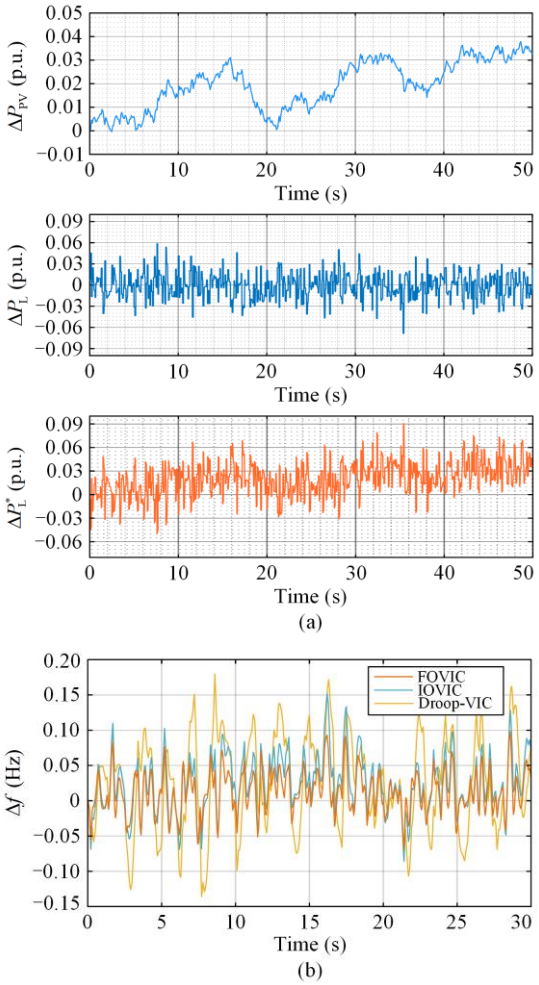

Fig. 13. (a) Profiles of domestic load, solar-power generation, and their aggregation. (b) Frequency response of the studied power system under different optimized controllers.

C. Controller-robustness Analysis

The robustness of the controller is evaluated in the case of perturbations in the power-system parameters including M, D, and τ. The values of the objective function J under different parameter-perturbation cases are summarized in Table IV, and the corresponding system frequency responses are presented in Fig. 14. The results indicate that the FOVIC outperforms the droop VIC and IOVIC in terms of J values and frequency-response performance in most cases. This highlights the superior robustness of the FOVIC in the frequency regulation of a low-inertia system with uncertainty in the system parameters. Notably, the J values of the two VICs exceed that of the FOVIC when τ decreases by 50%. This may be attributed to the fact that component d in the objective function increases sharply as the stability region expands, and its centroid consequently moves away from the set parameters. The results in Fig. 14 also indicate that the perturbations in the mechanical inertia of the system M and communication time delay τ have a significant impact on system dynamics.

TABLE IV
ROBUSTNESS FOR PERTURBATION IN SYSTEM PARAMETERS

System parameters	Perturbation	Controller	J for increase in parameter	J for decrease in parameter
M	±30%	Droop VIC	0.0078	0.0182
		IOVIC	0.0032	0.0044
		FOVIC	0.0026	0.0032
D	±20%	Droop VIC	0.0082	0.0087
		IOVIC	0.0056	0.0029
		FOVIC	0.0046	0.0026
τ	±50%	Droop VIC	0.0114	0.0072
		IOVIC	0.0082	0.0093
		FOVIC	0.0068	0.0097

In addition, to further illustrate how the proposed tuning method enhances the robustness of FOVIC, we consider a scenario in which a 110 MW generator trips. The responses of the two parameter setpoints (J_v, D_v, v) of the FOVIC are compared, which are (20, 20, 0.5) and (22, 28, 0.5). Before a fault occurs, the frequency-regulation performance of the FOVIC under set-point B is better than that under set-point A as it has higher parameter values. Higher controller-parameter set-points are typically preferred to obtain a better frequency-regulation performance. However, in the proposed parameter-tuning method, as depicted in Fig. 15, the robustness is quantized as the distance from the centroid to the parameter setpoint. The closer the setpoint is to the centroid, the less unlikely it is to fall out of the stability region. The proposed method considers robustness and selects a relatively conservative parameter setpoint, reaching a tradeoff between frequency-regulation performance and controller robustness.

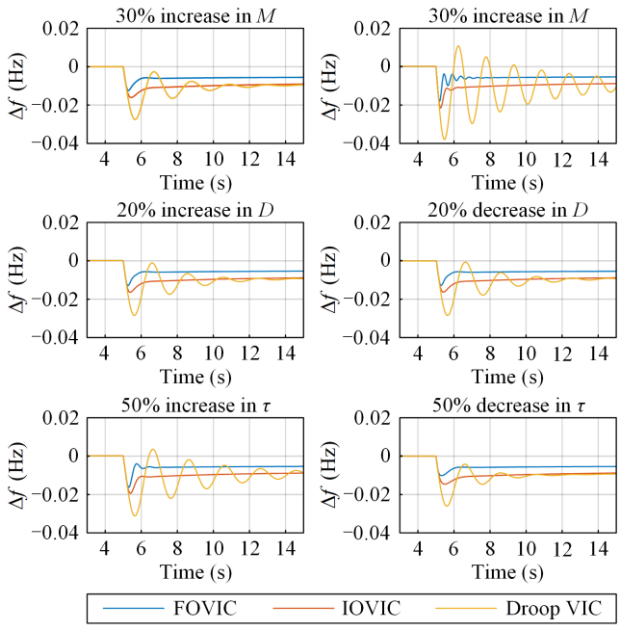

Fig. 14. Frequency response of the power system subject to different parameter perturbations.

After the generator fault, an active power deficit of 0.11 p.u. immediately occurs (the generator is assumed to generate its maximum power). Moreover, the participation factor of the thermal power plant P_{th} and system inertia M decrease to 0.44 and 4.3 s, respectively. Consequently, the stability region of FOVIC in Fig. 15 shrinks, and set-point A, with higher parameter values, is likely to fall out of the stability region. By contrast, set-point B remains within the stability region, demonstrating its robustness in the case of a large disturbance. The simulation results shown in Fig. 16 further verify this. After the generator trips, the frequency is unstable at set-point A but converges at set-point B.

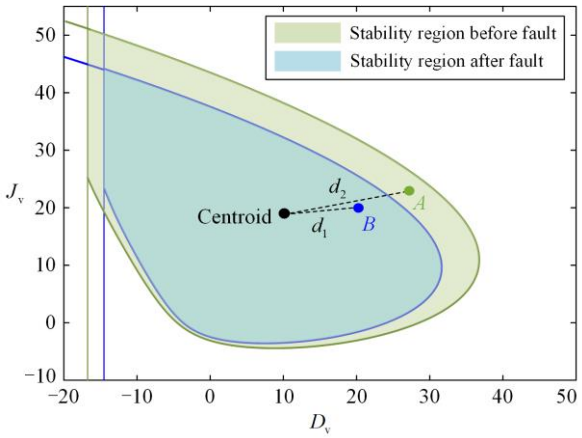

Fig. 15 Stability region before and after the generator fault.

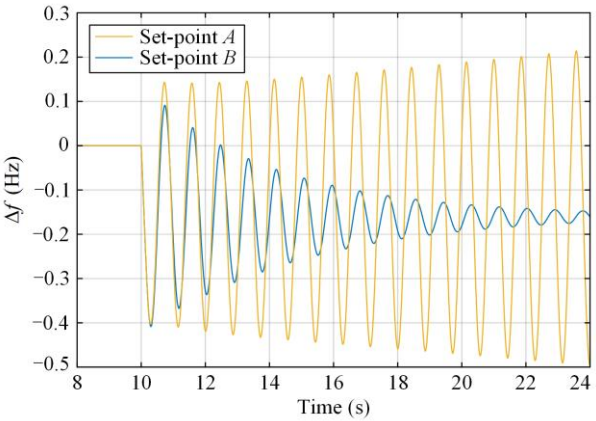

Fig. 16. Frequency response after fault under different parameter setpoints.

VI. CONCLUSION

This study proposes an FOVIC controller and a novel parameter-tuning method for a BESS to provide an FFR service for a lower-inertia power grid. The parameter-tuning method identifies the stability region in the parameter space and optimizes the parameters of the FOVIC to better suppress frequency deviation and enhance system robustness. The time-domain simulation results confirm that the identified stability region is

correct and demonstrate the superiority of the FOVIC in the frequency-regulation performance. The robustness of the FOVIC tuned using the proposed method is verified through case studies of parametric perturbation and generator faults in the power system.

However, this study has some limitations. In this study, the system frequency is deemed a global variable and remains uniform in all parts of the power system. In fact, a large disturbance can lead to multimodal oscillations, and the frequencies and ROCOF of different buses may differ significantly. In addition, when the stability region expands with a change in the system-operation status, the formerly selected parameter values become too conservative and weaken the controller performance.

Efforts must be made to improve the proposed method. For power systems with complicated networks, the system-response model must consider the effects of power flow. An online tuning method with a real-time stability region is desirable to achieve better frequency-regulation performance. Moreover, a novel FOVIC combining the advanced FOC techniques in [16] and [17] with the proposed parameter-tuning method should also be investigated.

ACKNOWLEDGMENT

Not applicable.

AUTHORS' CONTRIBUTIONS

Yukai Zeng: conceptualization, methodology, formal analysis, and writing original draft. Qiufan Yang: investigation and data curation. Yujun Lin: validation and visualization. Yin Chen: supervision. Xia Chen: writing, reviewing and editing. Jinyu Wen: funding acquisition, writing, reviewing and editing.

FUNDING

This work is supported by the Science and Technology Project of State Grid Corporation of China (No. 5419-202199551A-0-5-ZN), the Joint Funds of the National Natural Science Foundation of China (No. U22A6007), and the National Excellent Youth Science Fund Project of National Natural Science Foundation of China (No. 52222703).

AVAILABILITY OF DATA AND MATERIALS

Not applicable.

DECLARATIONS

Competing interests: The authors declare that they have no known competing financial interests or personal relationships that could have appeared to influence the work reported in this article.

AUTHORS' INFORMATION

Yukai Zeng received the B.S. degree in electrical engineering from South China University of Techonogy, Guangzhou, China, in 2021. He is currently persuing the M.S. degree in electrical engineering at Huazhong University of Science and Technology. His research interests include operation and control of battery energy storage in power system.

Qiufan Yang received the B.S. degree in electrical engineering from Huazhong University of Science and Technology (HUST), Wuhan, China, in 2019. He is currently working toward his Ph.D. degree in electrical engineering at HUST, Wuhan, China. His current research interests include DC microgrids, distributed control, and energy storages technologies.

Yujun Lin received the B.S. degree in electrical engineering from Chongqing University, Chongqing, China, in 2020. He is currently working toward the Ph.D. degree in electrical engineering with the Huazhong University of Science and Technology, Wuhan, China. His research interests include the distributed control and optimization of energy storage clusters.

Yin Chen received the B.S. degree in electrical engineering from the Huazhong University of Science and Technology, Wuhan, China, in 2009, the M.S. degree in electrical engineering from Zhejiang University, Hangzhou, China, in 2014, and the Ph.D. degree in electrical engineering from the University of Strathclyde, Glasgow, U.K., in 2020. He is currently a post-doctoral researcher with the University of Strathclyde. His research interests include the modeling of power electronic converters, grid integration of renewable power, and stability analysis of the HVDC transmission systems.

Xia Chen received the B.S. degree in power system and its automaton from Wuhan University of Technology, China, in 2006, and the M.S. and Ph.D. degrees in electrical engineering from Huazhong University of Science and Technology (HUST), China, in 2008 and 2012, respectively. She was a post-doctoral research fellow with the University of Hong Kong, from 2012 to 2015. In 2015 she joined the HUST and now she is a professor with the School of Electrical and Electronic Engineering, HUST. Her research interests include energy storage control and operation, renewable energy integration technologies, and new smart grid device.

Jinyu Wen received the B.E. and Ph.D. degrees all in electrical engineering from Huazhong University of Science and Technology (HUST), Wuhan, China, in 1992 and 1998, respectively. He was a visiting student from 1996 to 1997 and research fellow from 2002 to

2003 all at the University of Liverpool, UK, and a senior visiting researcher at the University of Texas at Arlington, USA in 2010. From 1998 to 2002 he was a director engineer in XJ Electric Co. Ltd. in China. In 2003 he joined the HUST and now is a professor at HUST. His current research interests include renewable energy integration, energy storage application, DC grid, and power system operation and control.

REFERENCES

[1] P. Tielens and D. V. Hertem, "The relevance of inertia in power systems," *Renewable and Sustainable Energy Review*, vol. 55, pp. 999-1009, 2016.

[2] F. Milano, F. Dörfler and G. Hug *et al.*, "Foundations and challenges of low-inertia systems," in *2018 IEEE Power Systems Computation Conference*, Dublin, Ireland, Jun. 2018, pp. 37-61.

[3] Z. Li, P. Zhou, and P. Chen *et al.*, "Key technologies research and application of a dynamic test for coordination controller of an electrochemical energy storage power station," *Power System Protection and Control*, vol. 51, no. 4, pp. 165-173, Feb. 2023. (in Chinese)

[4] X. Wang, M. G. Taul, and H. Wu *et al.*, "Grid-synchronization stability of converter-based resources—an overview," *IEEE Open Journal of Industrial Applications*, vol. 1, pp. 115-134, Aug. 2020.

[5] H. Wu, X. Ruan, and D. Yang *et al*., "Small-signal modeling and parameters design for virtual synchronous generators," *IEEE Transactions on Industrial Electronics*, vol. 63, no. 7, pp. 4292-4303, Mar. 2016.

[6] Q. Zhong and G. Weiss, "Synchronverters: inverters that mimic synchronous generators," *IEEE Transactions on Industrial Electronics*, vol. 58, no. 4, pp. 1259-1267, Apr. 2011.

[7] P. Saxena, N. Singh, and A. K. Pandey, "Self-regulated solar PV systems: replacing battery via virtual inertia reserve," *IEEE Transactions on Energy Conversion*, vol. 36, no. 3, pp. 2185-2194, Jan. 2021.

[8] T. Kerdphol, F. S. Pahman, and M. Watanabe *et al.*, "Model predictive control for virtual inertia synthesis," in *Virtual Inertia Synthesis and Control*, Cham, Switzerland: Springer International Publishing, 2021, pp. 141-166.

[9] Y. Yoo, S. Jung, and G. Jang, "Dynamic inertia response support by energy storage system with renewable energy integration substation," *Journal of Modern Power System and Clean Energy*, vol. 8, no. 2, pp. 260-266, Nov. 2020.

[10] V. Knap, R. Sinha, and M. Swierczynski *et al.*, "Grid inertial response with lithium–ion battery energy storage systems," in *2014 IEEE 23rd International Symposium on Industrial Electronics*, Istambul, Turkey, Jun. 2014, pp. 1817-1822.

[11] B. Yildirim, M. Gheisarnejad, and M. H. Khooban, "A new parameter tuning technique for non-integer Controllers in low-inertia modern power grids," *IEEE Journal of Emerging and Selected Topics in Power Electronics*, vol. 3, no.2, pp. 279-288, Oct. 2022.

[12] Y. Yu, Y. Guan and W. Kang *et al*., "Fractional-order virtual synchronous generator," *IEEE Transactions on Power Electronics*, vol. 38, no. 6, pp. 6874-6879, Jun. 2023.

[13] D. Li, K. Ding, and Y. Xia *et al*., "Research on fractional order modeling and PI^{λ} control strategy of V2G two-stage bidirectional converter," *IEEE Open Journal of Power Electronics*, vol. 4, pp. 716-726, Feb. 2023.

[14] B. Long, W. Zeng, and J. Rodríguez *et al*., "Enhancement of voltage regulation capability for DC-microgrid composed by battery test system: a fractional-order virtual inertia method," *IEEE Transactions on Power Electronics*, vol. 37, no. 10, pp. 12538-12551, Oct. 2022.

[15] D. Pullaguram, S. Mishra, and N. Senroy *et al.*, "Design and tuning of robust fractional order controller for autonomous microgrid VSC system," *IEEE Transactions on Industrial Applications*, vol. 54, no. 1, pp. 91-101, Oct. 2018.

[16] A. Zafari, M. Mehrasa, and S. Bacha *et al.*, "A robust fractional-order control technique for stable performance of multilevel converter-based grid-tied DG Units," *IEEE Transactions on Industrial Applications*, vol. 69, no. 10, pp. 10192-10201, Oct. 2022.

[17] V. Skiparev, K. Nosrati, and A. Tepljakov *et al.*, "Virtual inertia control of isolated microgrids using an NN-based VFOPID controller," *IEEE Transactions on Sustainable Energy*, vol. 14, no. 3, pp. 1558-1568, Jul. 2023.

[18] G. Tzounas, I. Dassios, and M. A. A. Murad *et al.*, "Theory and implementation of fractional order controllers for power system applications," *IEEE Transactions on Power System*, vol. 35, no.6, pp. 4622-4631, Nov. 2020.

[19] M. Barakat, "Novel chaos game optimization tuned-fractional-order PID fractional-order PI controller for load-frequency control of interconnected power systems," *Protection and Control of Modern Power Systems*, vol. 7, no. 2, pp. 1-20, Apr. 2022.

[20] M. V. Kazemi, S. J. Sadati, and S. A. Gholamian, "Adaptive frequency control of microgrid based on fractional order control and a data-driven control with stability analysis," *IEEE Transactions on Smart Grid*, vol. 13, no.1, pp. 381-392, Sept. 2022.

[21] S. Sönmez and S. Ayasun, "Stability region in the parameter space of PI controller for a single-area load frequency control System With Time Delay," *IEEE Transactions on Power System*, vol. 31, no. 1, pp. 829-830, Mar. 2016.

[22] K.Zare, M. H. Hagh, and J. Morsali, "Effective oscillation damping of an interconnected multi-source power system with automatic generation control and TCSC," *International Journal of Electric Power and Energy System*, vol. 65, pp. 220-230, Feb. 2015.

[23] Q. Shi, F. Li, and H. Cui, "Analytical method to aggregate multi-machine SFR model with applications in power system dynamic studies," *IEEE Transactions on Power System*, vol. 33, no. 6, pp. 6355-6367, Nov. 2018.

[24] A. González-Cajigas, J. Roldán-Pérez, and E. J. Bueno, "Design and analysis of parallel-connected grid-forming virtual synchronous machines for island and grid-connected applications," *IEEE Transactions on Power Electronics,* vol. 37, no. 5, pp.5107-5121, May 2022.

[25] G. Magdy, G. Shabib, and A. A. Elbaset *et al*., "Renewable power systems dynamic security using a new coordination of frequency control strategy based on virtual synchronous generator and digital frequency protection," *International Journal of Electric Power and Energy System*, vol. 109, pp. 351-368, Jul. 2019.

[26] Y. Zuo, Z. Yuan, and F. Sossan *et al.*, "Performance assessment of grid-forming and grid-following converter-interfaced battery energy storage systems on frequency regulation in low-inertia power grids," *Sustainable Energy*, *Grids and Networks*, vol. 27, Sept. 2021.

[27] A. Berizzi, A. Bosisio, and V. Ilea *et al.*, "Analysis of synthetic inertia strategies from wind turbines for large system stability," *IEEE Transactions on Industrial Applications*, vol. 58, no. 3, pp. 3184-3192, May 2022.

[28] S. Eberlein and K. Rudion, "Impact of inner control loops on small-signal stability and model-order reduction of grid-forming converters," *IEEE Transactions on Smart Grid*, vol. 14, no. 4, pp. 2812-2824, Jul. 2023.

[29] E. Rakhshani and P. Rodriguez, "Inertia emulation in AC/DC interconnected power systems using derivative technique considering frequency measurement effects," *IEEE Transactions on Power Systems*, vol. 32, no. 5, pp. 3338-3351, Sept. 2017.

[30] N. B. Lai, A. Tarraso, and G. N. Baltas *et al*, "Inertia emulation in power converters with communication delays," in *2020 IEEE Energy Conversion Congress and Exposition*, Detroit, USA, Oct. 2020, pp. 1665-1669.

[31] ABB, (2015 Apr. 9), "Wind turbine converters," [Online].Available:https://new.abb.com/power-converters-inverters/wind-turbines.

[32] V. C. Mathebula and A. K. Saha, "Reliability of IEC 61850 based substation communication network architecture considering quality of repairs and common cause failures," *Protection and Control of Modern Power Systems*, vol. 7, no. 1, pp. 1-15, Jan. 2022.

[33] J. Sabatier, P. Lanusse, and P. Melchior *et al*., "*Fractional order models*," in *Fractional Order Differentiation and Robust Control Design in Intelligent Systems*, *Control and Automation*: *Science and Engineering*, Dordrecht, The Netherlands: Springer, 2015, pp. 1-61.

[34] D. Xue, "Definition and calculation of fractional order calculus," in *Fractional Calculus and Fractional-order Control*, Beijing, China: Science Press, 2018, pp. 33-40. (in Chinese)

[35] M. Buslowicz, "Stability of linear continuous-time fractional order systems with delays of the retarded type," *Bulletin of the Polish Academy of Sciences*, vol. 56, no. 4, pp. 319-324, Dec. 2008.

[36] A. J. Guel-Cortez, C. F. Méndez-Barrios, and E. J. González-Galván, "Geometrical design of fractional PD^{μ} controllers for linear time-invariant fractional-order systems with time delay," *Journal of System and Control Engineering*, vol. 233, no. 7, pp. 815-829, Jan. 2019.

[37] N. Hatziargyriou, J. V. Milanović, and C. Rahman *et al.*, "Stability definitions and characterization of dynamic behavior in systems with high penetration of power electronic interfaced technologies," Power System Dynamic Performance Committee (PSDP), Piscataway, NJ, IEEE PES Technical Report PES-TR77, 2020.

[38] P. Bourke, (1997 July 5), "Calculating the area and centroid of a polygon," [Online].Available:http://paulbourke.net/geometry/polygonmesh/

[39] J. Cao and B. Cao, "Design of fractional order controllers based on particle swarm optimization," in *2006 1ST IEEE Conference on Industrial Electronics and Applications*, Singapore, Singapore, May 2006, pp. 775-781.